

Modeling of 3D trajectory of Hayabusa2 re-entry based on acoustic observations

Yasuhiro Nishikawa, Masa-Yuki Yamamoto, Eleanor K. Sansom, Hadrien A. R. Devillepoix, Martin C. Towner, Yoshihiro Hiramatsu, Taichi Kawamura, Kazuhisa Fujita, Makoto Yoshikawa, Yoshiaki Ishihara, et al.

▶ **To cite this version:**

Yasuhiro Nishikawa, Masa-Yuki Yamamoto, Eleanor K. Sansom, Hadrien A. R. Devillepoix, Martin C. Towner, et al.. Modeling of 3D trajectory of Hayabusa2 re-entry based on acoustic observations. Publications of the Astronomical Society of Japan, 2022, pp.758-775. 10.1093/pasj/psab126 . insu-03584322

HAL Id: insu-03584322
https://insu.hal.science/insu-03584322

Submitted on 22 Feb 2022

HAL is a multi-disciplinary open access archive for the deposit and dissemination of scientific research documents, whether they are published or not. The documents may come from teaching and research institutions in France or abroad, or from public or private research centers.

L'archive ouverte pluridisciplinaire **HAL**, est destinée au dépôt et à la diffusion de documents scientifiques de niveau recherche, publiés ou non, émanant des établissements d'enseignement et de recherche français ou étrangers, des laboratoires publics ou privés.



Distributed under a Creative Commons Attribution 4.0 International License

Publ. Astron. Soc. Japan (2022) 00 (0), 1–10
https://doi.org/10.1093/pasj/psab126
Advance Access Publication Date: 2022 0

Modeling of 3D trajectory of Hayabusa2 re-entry based on acoustic observations

Yasuhiro Nishikawa [1,*] Masa-yuki Yamamoto,[1] Eleanor K. Sansom [2] Hadrien A. R. Devillepoix,[2] Martin C. Towner,[2] Yoshihiro Hiramatsu,[3] Taichi Kawamura,[4] Kazuhisa Fujita,[5] Makoto Yoshikawa,[5] Yoshiaki Ishihara,[6] Islam Hamama,[7,8] Norihisa Segawa,[9] Yoshihiro Kakinami,[10] Hiroshi Katao,[11] Yuichiro Inoue,[7] and Philip A. Bland[2]

[1]School of System Engineering, Kochi University of Technology, 185 Miyanokuchi, Tosayamada, Kami, Kochi 782-8502, Japan
[2]Space Science and Technology Centre, Curtin University, Kent Street, Bentley, Perth, WA, Australia
[3]School of Geosciences and Civil Engineering, College of Science and Engineering, Kanazawa University, Kakuma-machi, Kanazawa, Ishikawa 920-1192, Japan
[4]Institut de Physique du Globe de Paris, 35 Rue Hélène Brion, Paris 75013, France
[5]Institute of Space and Astronautical Science, Japan Aerospace Exploration Agency, 3-1-1 Yoshinodai, Chuo-ku, Sagamihara-shi, Kanagawa 252-5210, Japan
[6]JAXA Space Exploration Center, Japan Aerospace Exploration Agency, 3-1-1 Yoshinodai, Chuo-ku, Sagamihara-shi, Kanagawa 252-5210, Japan
[7]Graduate School of Engineering, Kochi University of Technology, 185 Miyanokuchi, Tosayamada, Kami, Kochi 782-8502, Japan
[8]National Research Institute of Astronomy and Geophysics, Helwan 11421, Cairo, Egypt
[9]Faculty of Information Center Science and Engineering, Kyoto Sangyo University, Motoyama, Kamigamo, Kita-ku, Kyoto, Kyoto 603-8555, Japan
[10]Space Information Center, Hokkaido Information University, 59-2 Nishi-nopporo, Ebetsu, Hokkaido 069-0832, Japan
[11]Research Center for Earthquake Prediction, Disaster Prevention Research Institute, Kyoto University, Gokasho, Uji, Kyoto 611-0011, Japan

*E-mail: nishikawa.yasuhiro@kochi-tech.ac.jp

Received 2021 November 23; Accepted 2021 December 16

Abstract

On 2020 December 5 at 17:28 UTC, Japan Aerospace Exploration Agency's Hayabusa2 sample return capsule (SRC) re-entered Earth's atmosphere. The capsule passed through the atmosphere at supersonic speeds, emitting sound and light. The inaudible sound was recorded by infrasound sensors installed by Kochi University of Technology and Curtin University. Based on analysis of the recorded infrasound, the trajectory of the SRC in two cases, one with constant-velocity linear motion and the other with silent flight, could be estimated with an accuracy of 0.°5 in elevation and 1° in direction. A comparison with optical observations suggests a state of flight in which no light is emitted but

© The Author(s) 2022. Published by Oxford University Press on behalf of the Astronomical Society of Japan. This is an Open Access article distributed under the terms of the Creative Commons Attribution License (http://creativecommons.org/licenses/by/4.0/), which permits unrestricted reuse, distribution, and reproduction in any medium, provided the original work is properly cited.

Downloaded from https://academic.oup.com/pasj/advance-article/doi/10.1093/pasj/psab126/6527740 by CNRS - ISTO user on 22 February 2022

sound is emitted. In this paper, we describe the method and results of the trajectory estimation.

Key words: atmospheric effects — instrumentation: miscellaneous — method: observational — shock waves — space vehicles: instruments

1 Introduction

Meteoroids passing through the atmosphere at supersonic speeds generate shock waves (ReVelle 1976). Studies have calculated the trajectories of fireball (bright meteors) from seismometer measurements of the associated shock waves (Nagasawa 1987; Ishihara et al. 2003, 2004). Re-entry capsules passing through the atmosphere also generate shock waves, as observed for Stardust (Desai et al. 1999; ReVelle & Edwards 2007), Genesis (ReVelle et al. 2005) and Hayabusa (Yamamoto et al. 2011; Ishihara et al. 2012) during their atmospheric re-entry. It has been suggested that it may be possible to estimate the trajectory and speed of an object from measurements of the sound it emits (Lonzaga et al. 2015). The asteroid explorer Hayabusa2, launched by the Japan Aerospace Exploration Agency (JAXA) on 2014 December 3, arrived at the asteroid Ryugu in 2018 and collected surface rocks during two touch downs (on 2019 February 22 and July 11) (Tsuda et al. 2019, 2020). The collected samples were stored in a sample return capsule (SRC), which re-entered Earth's atmosphere at around 17:28 (UTC) on 2020 December 5, and successfully landed in South Australia. Infrasound sensors (INF04LE micro-atmospheric vibrometers, see below) at seven sites (four sensors at each site, for a total of 28 sensors) along the re-entry trajectory (figure 1) installed by Kochi University of Technology, Japan, and Curtin University, Australia, detected the infrasound generated by the SRC as it passed through the atmosphere. Many infrasound sensors were deployed to establish a temporary sensor network. At the time of the Hayabusa1 re-entry in 2010, we deployed only five infrasound sensors (Model 2 and Model 25, Chaparral Physics).

Since then, we have been developing original infrasound sensors in collaboration with a manufacturing company (SAYA Inc., Japan). A small chamber electromagnetically coupled to simple membranes is used to measure sounds in the range of 6.25 Hz down to 0.001 Hz (SAYA INF01LE) and multiple capacitance microphones are used to measure sounds in the range of 0.05 Hz up to the audible range (SAYA INF04LE). Since 2016, the INF01LE sensors have been deployed in Japan to monitor meteorologically and/or event-driven variation of infrasound to estimate the energy deposition of geophysical events such as tsunamis, volcanic eruptions, and thunderstorms, and its propagation characteristics in the atmosphere (Batubara & Yamamoto 2020; Hamama & Yamamoto 2021; Saito et al. 2021). The data from the 28 INF04LE sensors, which are portable and have low power consumption, used in this study were recorded by Raspberry Pi data loggers (Sansom et al. 2022). The numbering of the locations of the infrasound sensors used here follows that used by Sansom et al. (2022), where the seven locations are numbered from 2 to 8. At a given location, one sensor was placed at the center and the other three sensors were placed at the vertices of an equilateral triangle, each 100 m from the center. The time of arrival of a shock wave depends on the location of the installed infrasound sensor. It is recorded by the sensor as an N-type signal (Langston 2004), as shown in figure 2.

In this study, the return trajectory and behavior of the SRC in the atmosphere were determined by comparing the observed infrasound data with the calculated arrival time of the shock wave. Based on a comparison of the calculated wavefronts with the locations of the infrasound sensors, we suggest the possibility of silent flight (here we refer to the flight of a fireball that is acoustically silent as silent flight, because there is a state in which the fireball is emitting sound; see subsection 4.3) and propose more accurate descriptions of the SRC behavior in the atmosphere and the propagation of shock wavefronts by taking into account the effect of silent flight. In general, the flight of a fireball without the emission of light is called dark flight. Past studies have not clearly differentiated between the inaudible (silent) and invisible (dark) flights.

2 Method

Usually, the shape of a shock wave can be simply determined from the speed of sound and that of the supersonic object, which are obtained from the arrival times of sound waves recorded by multiple infrasound sensors distributed on the ground. The speed of sound is uniform [305 ($m\,s^{-1}$) in this study] because of the shallow entry angle of the SRC. Under the assumption that the speeds of sound and the object are constant during the descent, the shape of the wavefront can be treated as a cone (Mach cone). Hayabusa2 passing through the upper atmosphere at a shallow angle is

Downloaded from https://academic.oup.com/pasj/advance-article/doi/10.1093/pasj/psab126/6527740 by CNRS - ISTO user on 22 February 2022

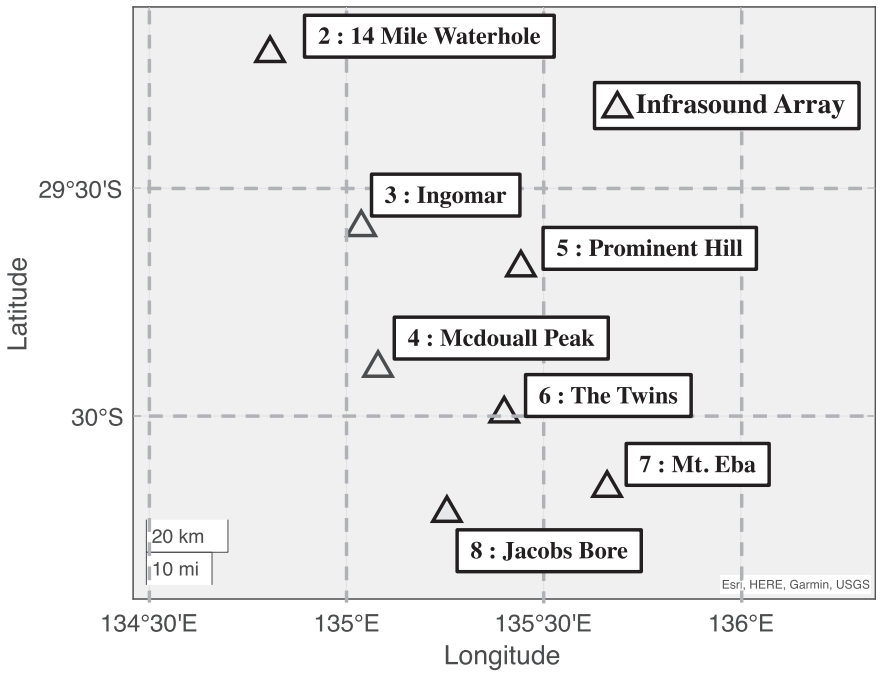


Fig. 1. Layout of infrasound sensors installed near nadir of the SRC re-entry trajectory.

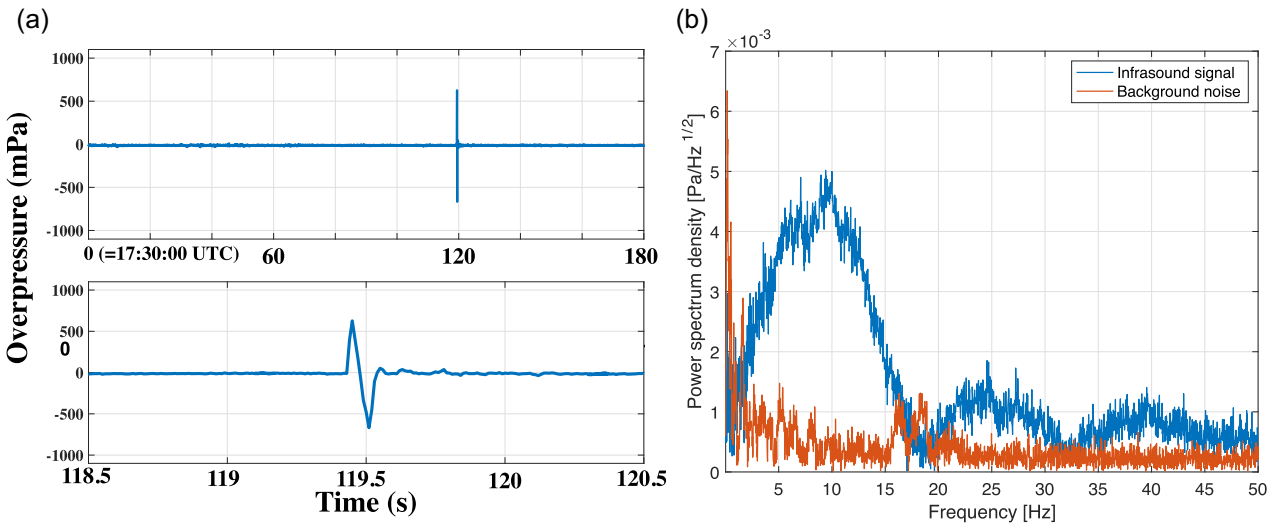


Fig. 2. Examples of observed infrasound, recorded in the 0.01–50 Hz band. (a) Overpressure versus time, at Jacobs Bore (30°21261S, 135°25473E), where the infrasound shock waves reached at around 119 s from 17:28:00 UTC, and magnified view of recorded N-type signal (bottom panel). (b) Power spectrum density of infrasound signal and background noise. The signal has a peak at 10 Hz. (Color online)

consistent with this assumption, which is thus adopted in this paper.

To simplify the description of the Mach cone equation, we introduce a new coordinate system in which one axis coincides with the trajectory of the SRC. Here we define a rectangular coordinate system (x, y, z) where the x, y, and z-axes are defined as the positive north, east, and zenith directions, respectively. The origin of (x, y, z) is set at a point 30°S and 135°E on the ground surface. We define another coordinate system, (X, Y, Z), by rotating and translating the (x, y, z) coordinate system (figure 3). The coordinate system (X, Y, Z) is expressed as

$$\begin{pmatrix} X \\ Y \\ Z \end{pmatrix} = \begin{pmatrix} \cos\gamma\sin\theta & \sin\gamma\sin\theta & -\cos\theta \\ -\sin\gamma & \cos\gamma & 0 \\ \cos\gamma\cos\theta & \sin\gamma\cos\theta & \sin\theta \end{pmatrix} \begin{pmatrix} x - x_0 \\ y - y_0 \\ z \end{pmatrix}, \tag{1}$$

where γ and θ are, respectively, the azimuth of the Z-axis (counterclockwise from the x-axis, N–S axis on the ground)

Downloaded from https://academic.oup.com/pasj/advance-article/doi/10.1093/pasj/psab126/6527740 by CNRS - ISTO user on 22 February 2022

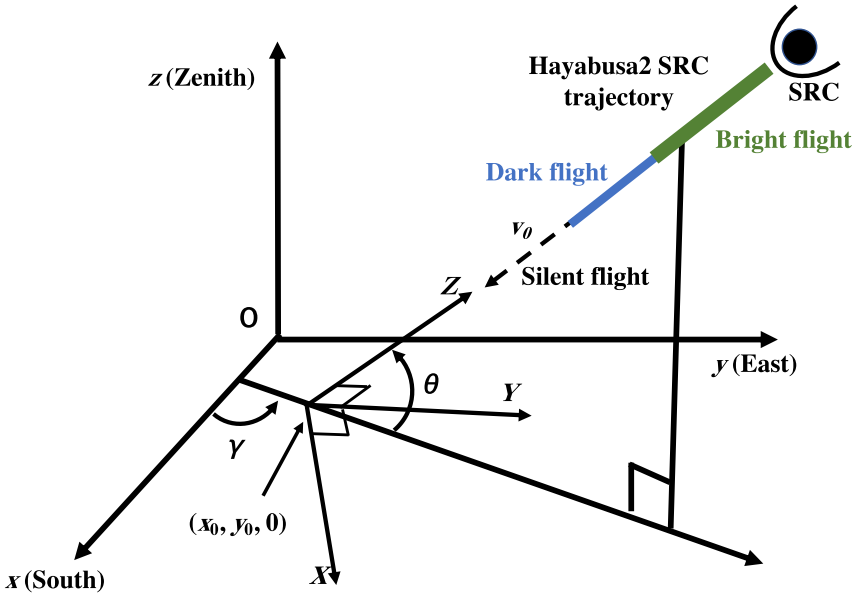


Fig. 3. Diagram of the (*X*, *Y*, *Z*) coordinate system, obtained by rotating and translating the (*x*, *y*, *z*) coordinate system. The *Z*-axis coincides with the trajectory of Hayabusa2 SRC. γ and θ are the cardinal direction and elevation angle, respectively. The trajectory is broken into three chunks: "bright flight", "dark flight", and "silent flight". Silent flight was observed to last one second longer than dark flight (see subsection 4.3). (Color online)

and the elevation angle of the trajectory from the *x*–*y* plane (ground plane). The matrix shows the rotation and x_0 and y_0 shown in the right-hand coordinates describe the parallel translation. Here, $(x_0, y_0, 0)$ is not the actual location of the capsule landing point, but the point of straight intersection with the ground where the capsule would have been if it had travelled in a constant-velocity linear motion toward the surface. The *Z*-axis indicates the direction of the trajectory of the Hayabusa2 capsule (figure 3).

The wavefront of the propagating infrasound at a given time t can be expressed by

$$[v_0(t_k - t_0) + Z_k] \tan\beta = \sqrt{X_k^2 + Y_k^2}, \tag{2}$$

where v_0, t, subscript k, t_0, and β are the velocity of the Hayabusa2 capsule, the arrival time of the shock wave, the number of the corresponding infrasound sensor (2 to 8 in this paper), the expected time for the capsule to reach the surface intersection $(x_0, y_0, 0)$, and the Mach angle ($\sin\beta = c_s/v_0$), respectively. In reality, the shock wavefront is not a cone because sound path is refracted, but this effect is so small that it will be ignored in this study.

If the six parameters of the SRC (v_0, x_0, y_0, γ, θ, and t_0) are fixed we can calculate the expected shock wave arrival time (t_k). The trajectory and arrival time are determined by equation (2) and the six free parameters, which we determined by minimizing the following χ^2 statistic:

$$\chi^2 = \sum \frac{(t_{\mathrm{calc},k} - t_{\mathrm{obs},k})^2}{t_{\mathrm{obs},k}}, \tag{3}$$

Table 1. Search domain, grid interval, and optimal value for each parameter.*

Parameter	Search domain	Grid interval	Optimal value	Error
v_0 (km s^{-1})	10 to 40	1.0	21	−4/+6
x_0 (km)	−600 to −200	1.0	−483	−7/+8
y_0 (km)	200 to −600	1.0	482	−7/+7
γ (°)	3 to 15	0.5	4.0	−0.5/+0.5
θ (°)	215 to 225	0.5	222.5	−0.5/+0.5
t_0 (s)	−50 to 50	1.0	22	−5/+5

*Origin is (30°S, 135°E, 0) at $17^h30^m00^s$ UTC.

where $t_{\mathrm{obs},k}$ and $t_{\mathrm{calc},k}$ are the observed and calculated times of arrival at the kth site. In this calculation the effect of wind is neglected, because the average wind speed in the atmosphere below 60 km altitude at the time is 5 (m s^{-1}) in the west and 0.2 (m s^{-1}) in the north direction. The difference in the location of the shock wave due to the wind effect is smaller than 1 (km) of a grid.

3 Results

We varied each parameter over a wide range and used the χ^2 test to find the optimal parameter set (table 1).

From these optimum values, the arrival wave lines of the shock wave and the trajectory of the SRC can be drawn as shown in figures 4 and 5.

Downloaded from https://academic.oup.com/pasj/advance-article/doi/10.1093/pasj/psab126/6527740 by CNRS - ISTO user on 22 February 2022

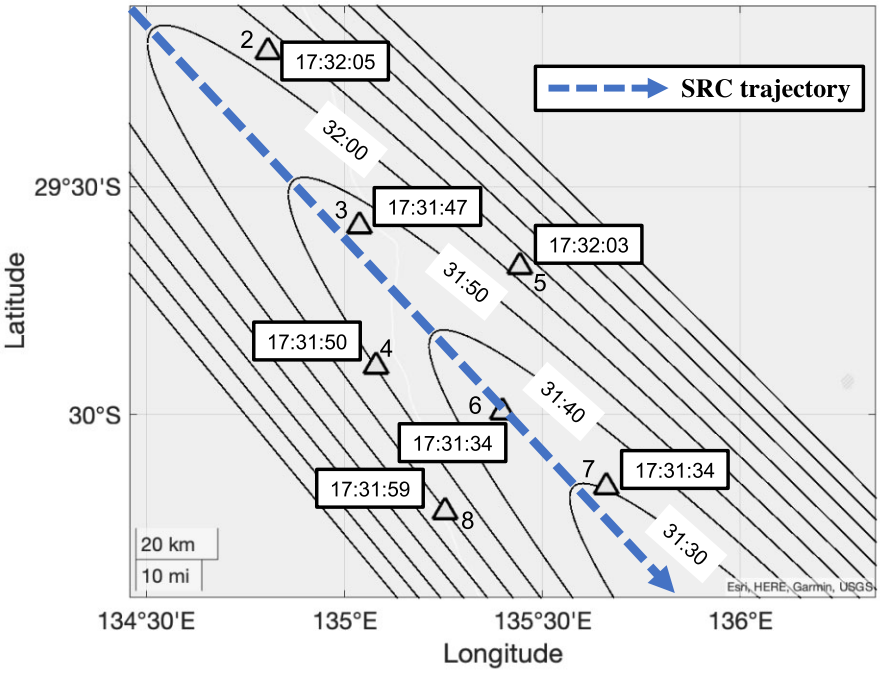


Fig. 4. Calculated propagation of shock wavefront projected on to the ground. The times in black frames indicate the arrival times of the shock wave at the corresponding sensors. The arrow indicates the SRC trajectory. The parabola shows the wavefront of the shock wave every 10 seconds. The times without black frames indicate the arrival times of the wavefront. The shape of the wavefront is an oblique cut on the surface of the Mach cone and is thus part of a parabola. Its direction of propagation is opposite to that of the descending SRC. (Color online)

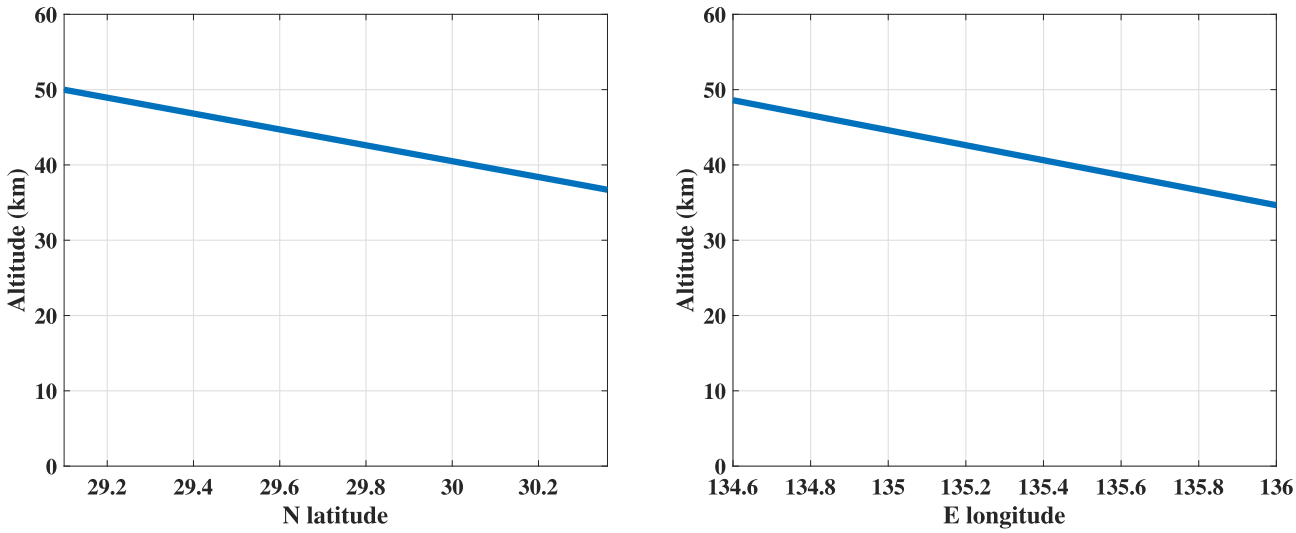


Fig. 5. Calculated elevation change of SRC. The SRC moves from northwest to southeast with an elevation angle of 4° and gradually loses altitude. It passes over the infrasound sensors at an altitude of about 35–50 km. (Color online)

Comparing the results of these calculations with the observations, the timing residuals are within three seconds at all observation points (table 2).

Although the error in the velocity (v_0) appears to be large, this can be explained by the fact that equation (2) is used for determining the shock wave surface. When v is sufficiently larger than the sound velocity (c_s), equation (2) can be rewritten as

$$t_k - t_0 = \frac{1}{v_0}\left(\frac{\sqrt{X_k^2 + Y_k^2}}{\tan\beta} - Z_k\right), \sim \frac{\sqrt{X_k^2 + Y_k^2}}{c_s} - \frac{Z_k}{v_0}. \quad (4)$$

Downloaded from https://academic.oup.com/pasj/advance-article/doi/10.1093/pasj/psab126/6527740 by CNRS - ISTO user on 22 February 2022

Table 2. Observed and calculated arrival times of shock waves.

Site number	Site	Observed	Calculated	Timing residual
2	14 Mile Waterhole	17:32:04.9	17:32:03.9	1.0
3	Ingomar	17:31:46.8	17:31:47.3	−0.5
4	Mcdouall Peak	17:31:50.5	17:31:49.5	1.0
5	Prominent Hill	17:32:02.9	17:32:03.5	−0.6
6	The Twins	17:31:33.8	17:31:36.2	−2.4
7	Mt. Eba	17:31:34.2	17:31:32.1	2.1
8	Jacobs Bore	17:31:59.3	17:31:59.2	0.1

Equation (4) shows that when v_0 is sufficiently larger than c_s, the arrival time of the shock wave t_k is only slightly affected by v_0 (even though X_k, Y_k, and Z_k are of the same order of magnitude, v_0 is sufficiently larger than c_s that the Z_k/v_0 is smaller than X_k/c_s and Y_k/c_s). Meteoroids and reentry objects are known to pass through the atmosphere at super sonic speeds (10–30 km s^{-1}). This means that it is difficult to determine the velocity of an object using the method described in this paper. However, because changing the object's velocity has almost no effect on the object's trajectory, shock wave surface, and shock wave arrival time, the method is effective for calculating the trajectory and arrival time of the shock wave.

4 Discussion

4.1 Silent flight effect

In this paper, trajectory calculations were performed using the grid-search-based method and the best values were obtained using the χ^2 test. The value of χ^2 was 0.133; however, if we ignore the data obtained at Mt. Eba (site no. 7), the value of χ^2 decreases sharply to 0.0012. This indicates that the handling of the data obtained at Mt. Eba was not appropriate. Mt. Eba is the most southeasternly site, and thus the last site that the capsule passed over. Therefore, any change in the behavior of the capsule just before it passed over Mt. Eba could explain the large error in the obtained data.

As long as the capsule is moving at supersonic speed through the atmosphere, the shock wave surface will be in the shape of a cone (in the case where the speed of sound is uniform and wind effect is small); however, when the capsule suddenly decelerates, the shock wave surface will be a sphere centered at the location where the sudden deceleration occurred. After entering the atmosphere, meteoroids usually slow down through melting and fragmentation (McCrosky & Ceplecha 1970). In contrast, the SRC, whose surface is ablated but does not melt or fragment, brakes suddenly where the density of the atmosphere increases rapidly (Ceplecha et al. 1998). After deceleration, the shock wave surface is not a cone, but a combination of a cone and a sphere (figure 6). In this case, equation (2) cannot be used to calculate the shock wave arrival time; thus a new equation is introduced. By including this silent flight effect in the calculation, we can explain the data obtained at Mt. Eba. In the defined (X, Y, Z) coordinate system, the shock wave surface is expressed as follows (Yamada & Mori 2012):

$$\left\{ \begin{array}{ll} [v_0(t_k - t_0) + Z_k]\tan\beta = \sqrt{X_k^2 + Y_k^2} & \text{if } Z_k \geq Z_D - r_D \sin\beta \\ r_D^2 = X_k^2 + Y_k^2 + (Z_k - Z_D)^2 & \text{if } Z_k < Z_D - r_D \sin\beta \end{array} \right\}, \tag{5}$$

$$Z_D = -t_D v_0, \tag{6}$$

$$r_D = c_s(t - t_D), \tag{7}$$

where Z_D, r_D, and t_D are, respectively, the value along the Z-axis at the location where the SRC is in silent flight, the radius of the spherical shock wave centered on the point where silent flight started (figure 6), and the time when silent flight started.

After the onset of silent flight, the shock wave is spherical, and thus the surface of the shock wave looks like a combination of a cone and a sphere. If the silent flight starts between The Twins and Mt. Eba, the shock wave that arrives at Mt. Eba may be delayed (figure 7). We searched for the optimal value in a similar way to the calculation of the penetration case (table 3). In this silent flight case, the value of χ^2 is 0.0084, which is smaller than 7% of that in penetration case. The calculated arrival times are thus likely to be closer to the observed arrival times in the silent flight case (table 4) compared to the penetration case (table 2).

According to this calculation, the dark flight started at an altitude of about 39 km, and the trajectory of the SRC after that start cannot be estimated (figure 8).

In this calculation, the trajectory is described more accurately because one infrasound sensor was affected by silent flight. If more than one sensor had been affected by silent flight, an even more accurate calculation could have been made.

Downloaded from https://academic.oup.com/pasj/advance-article/doi/10.1093/pasj/psab126/6527740 by CNRS - ISTO user on 22 February 2022

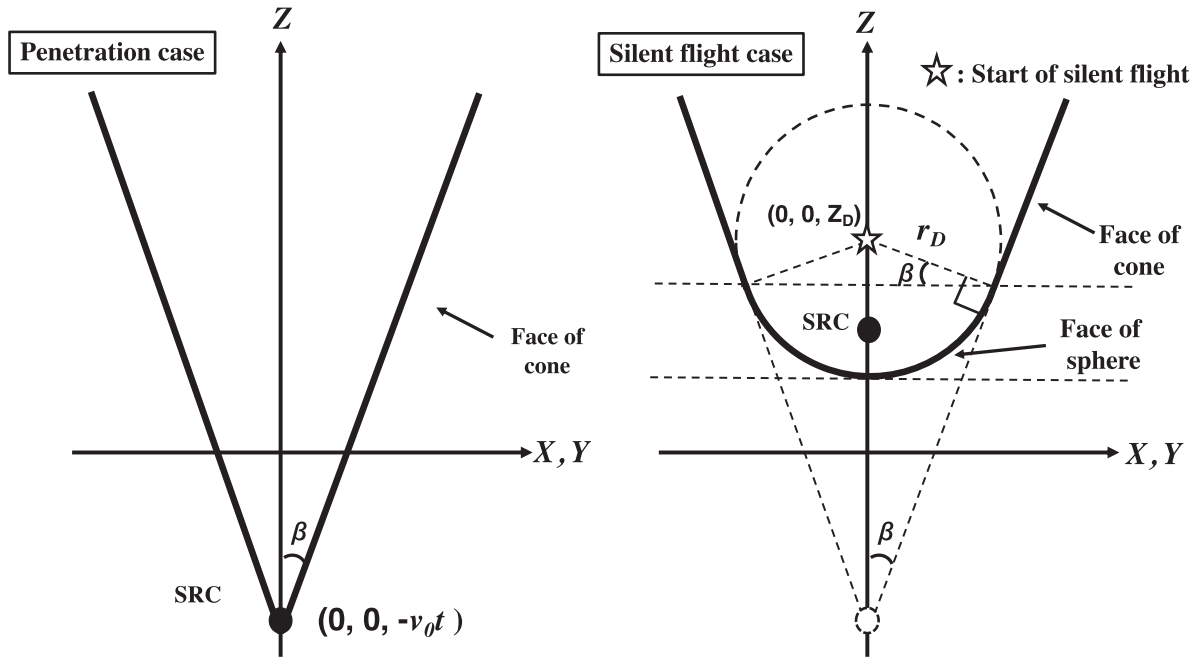


Fig. 6. Geometries of shock wave surface. In the penetration case, where the SRC continues its constant velocity linear motion, the shock wavefront is shaped like a cone. In the silent flight case, where the SRC decelerates rapidly at (0, 0, Z_D), the shock wavefront is shaped like a combination of a cone and a sphere.

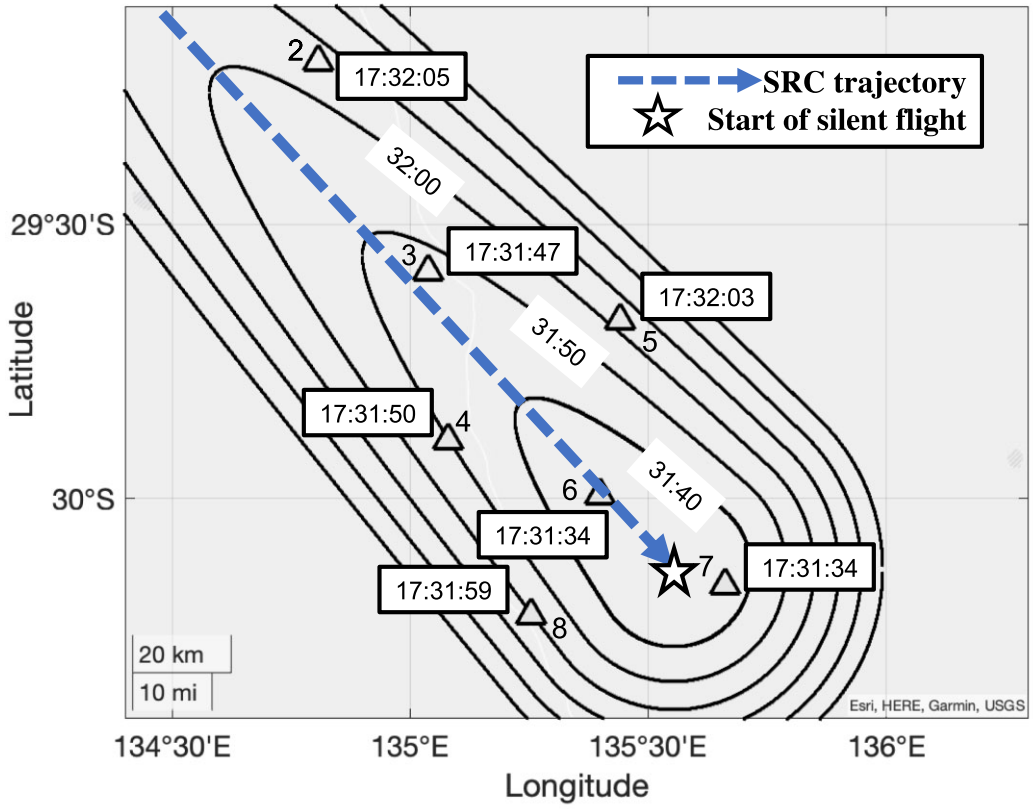


Fig. 7. Calculated propagation of shock wavefront in the silent flight case. The times in black frames indicate the arrival times of the shock wave at the corresponding sensors. The arrow indicates the SRC trajectory. The parabola shows the wavefront of the shock wave every 10 seconds. The times without black frames indicate the arrival times of the wavefront. The wavefronts of the shock wave are shaped like a combination of parabolas and circles. The silent flight began in the sky between the sixth (The Twins) and seventh (Mt. Eba) sensor sites. The error in this silent flight case is much smaller than that in the penetration case. (Color online)

Downloaded from https://academic.oup.com/pasj/advance-article/doi/10.1093/pasj/psab126/6527740 by CNRS - ISTO user on 22 February 2022

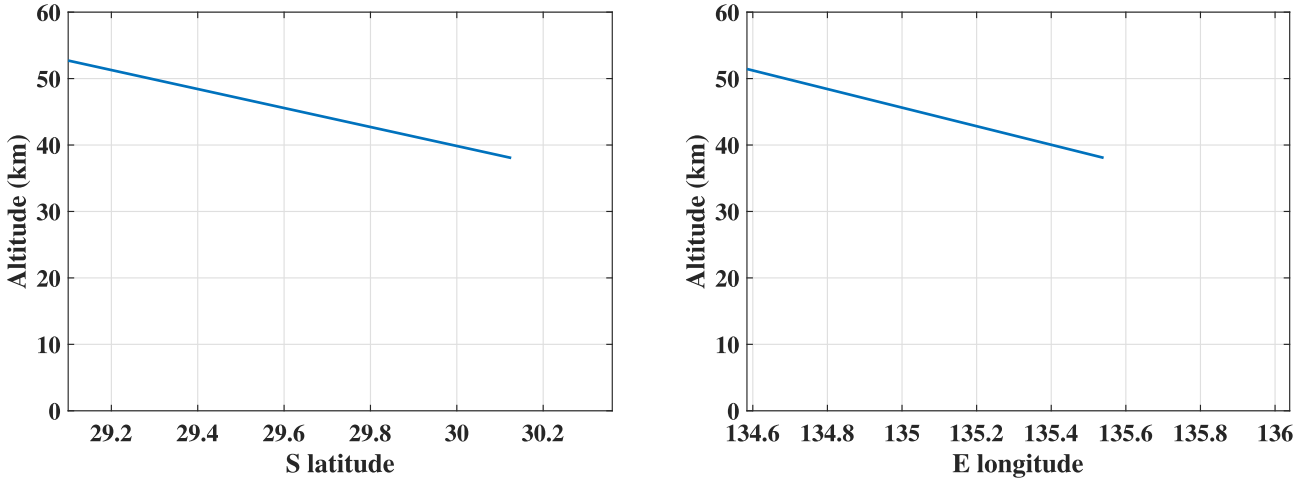


Fig. 8. Calculated elevation change of SRC. The SRC moves from northwest to southeast with an elevation angle of 5.5° and gradually loses altitude. It passes over the infrasound sensors at an altitude of about 53 km and transitions to silent flight at an altitude of about 39 km. The movement after the transition to silent flight cannot be inferred from the infrasound data. (Color online)

Table 3. Search domain, grid interval, and optimal value of each parameter for silent flight case.*

Parameter	Search domain	Grid interval	Optimal value	Error
v_0 (km s^{-1})	10 to 40	1.0	12	−3/+1
x_0 (km)	−600 to −200	1.0	−310	−8/+8
y_0 (km)	200 to 600	1.0	314	−7/+7
γ (°)	3 to 15	0.5	5.5	−0.5/+0.5
θ (°)	215 to 225	0.5	221.5	−1 /+1
t_0 (s)	−50 to 50	1.0	2	−6/+6
t_D (s)	−60 to 20	1.0	−33	−1/+1

*Origin is (30°S, 135°E, 0) at $17^h30^m00^s$ UTC.

Table 4. Observed and calculated arrival time of shock waves for silent case.

Site number	Site	Observed	Calculated	Timing residual
2	14 Mile Waterhole	17:32:04.9	17:32:04.7	0.2
3	Ingomar	17:31:46.8	17:31:47.0	−0.2
4	Mcdouall Peak	17:31:50.5	17:31:49.8	0.7
5	Prominent Hill	17:32:02.9	17:32:03.2	−0.3
6	The Twins	17:31:33.8	17:31:33.3	0.5
7	Mt. Eba	17:31:34.2	17:31:34.1	0.1
8	Jacobs Bore	17:31:59.3	17:31:59.2	0.1

4.2 Correction of elevation angle

According to JAXA's reporter briefing, the atmospheric interference for the SRC is about 200 km in altitude with an approach angle of 12° (JAXA Hayabusa2 Project 2020).[1]

[1] JAXA Hayabusa2 Project 2020, Reporter briefing: Asteroid explorer, Hayabusa2, ⟨https://www.hayabusa2.jaxa.jp/enjoy/material/press/Hayabusa2_Press_20201130_ver8_en2.pdf⟩.

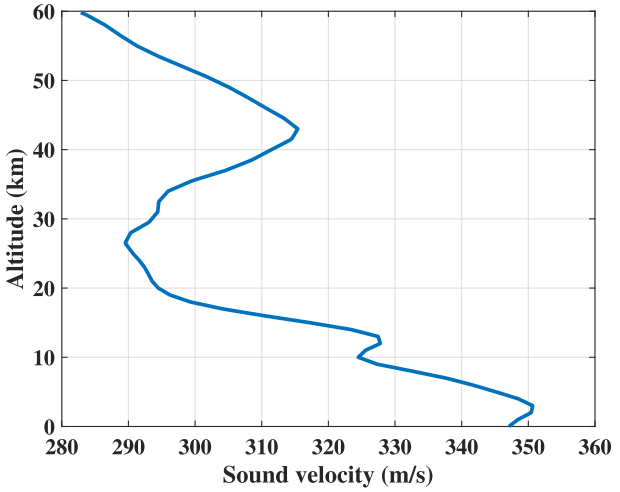


Fig. 9. Thermodynamic sound speed profile over sites of Hayabusa2 re-entry on ground. The profile was estimated using $c_{th} = \sqrt{\gamma RT}$ (Garcés et al. 1998), where γ (ratio of specific heats) =1.4, R (specific gas constant for dry air) =286.9 J kg^{-1} K^{-1} and temperature T were extracted from the MERRA-2 dataset.[2] (Color online)

This approach angle (12°) differs significantly from the elevation angle of 5° calculated in this study. This difference can be explained by the refraction of sound waves by the atmosphere and the roundness of Earth. When sound moves from a slower-velocity layer to a faster-velocity layer, the refraction angle becomes shallower and the elevation angle appears shallower than it should be. This effect is modified by the vertical structure of the atmosphere. The structure of the atmosphere above the SRC during re-entry is shown in figure 9. At an elevation angle of about 5°, the SRC is observed to have an elevation angle of about 0°.5–1°.0, smaller than it would be if the capsule had reached the ground from 40–60 km above.

Downloaded from https://academic.oup.com/pasj/advance-article/doi/10.1093/pasj/psab126/6527740 by CNRS - ISTO user on 22 February 2022

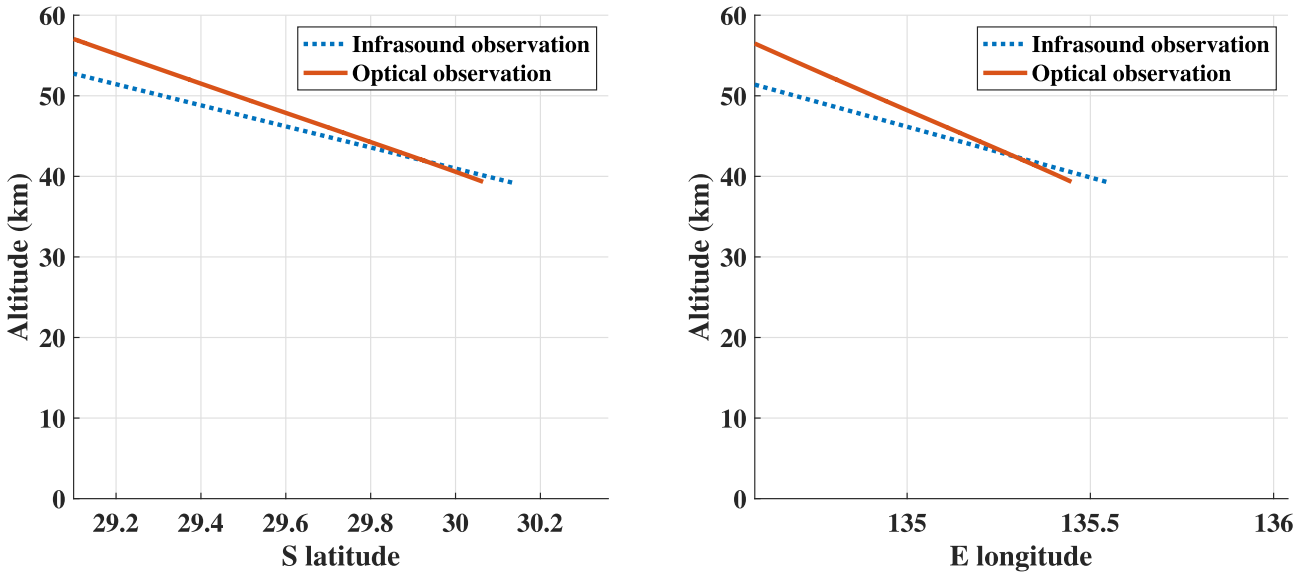


Fig. 10. Calculated elevation change of SRC. The blue dotted line and the red line are the trajectories determined from infrasound and optical observations, respectively. (Color online)

Table 5. Observed and calculated (based on optical trajectory) arrival times of the shock wave.

Site number	Site	Observed	Calculated	Infrasound delayed by 1 s
2	14 Mile Waterhole	17:32:04.9	17:32:06.5	17:32:04.5
3	Ingomar	17:31:46.8	17:31:48.2	17:31:47.0
4	Mcdouall Peak	17:31:50.5	17:31:49.2	17:31:49.9
5	Prominent Hill	17:32:02.9	17:32:04.3	17:32:03.1
6	The Twins	17:31:33.8	17:31:34.1	17:31:33.7
7	Mt. Eba	17:31:34.2	17:31:53.0	17:31:50.7
8	Jacobs Bore	17:31:59.3	17:31:56.3	17:31:59.4

Because Earth has a curvature, the angle at high altitude (γ_H) is larger than that at low altitude (γ_L) even if Earth is in constant-velocity linear motion. These angles are expressed by

$$\frac{\sin(90^\circ + \gamma_H)}{R_E + h_H} = \frac{\sin(90^\circ + \gamma_L)}{R_E + h_L}, \tag{8}$$

where R_E, h_H, and h_L are, respectively, the radius of Earth, a high-altitude position, and a low-altitude position. If an object is moving with constant-velocity linear motion from an altitude of 40 km to an elevation angle of 5° with respect to Earth, the elevation angle will be about 13.°5 at an altitude of 200 km. Considering these two effects, the elevation angle of 5.5° calculated in this study corresponds to 12.°5 at an altitude of 200 km, which is consistent with JAXA's reporter briefing.

4.3 Comparison with optical observation

We have thus far discussed only the sound data recorded by infrasound sensors. In this subsection, we compare the results with optical observations to verify their validity.

Kochi University of Technology and Curtin University detected infrasound generated by the SRC by installing a temporary scientific observation network under the expected trajectory. In addition to the infrasound sensors, cameras, seismic sensors, and antennas were installed. The trajectory estimated based on optical observations is similar to that estimated based on infrasound data (figure 10). The former was about 10 km ahead of the latter and was not visible (dark flight).

We calculated the shock wave arrival time at each observation site based on the optical trajectory. The results are shown in table 5. The arrival times are in good agreement except for that for Mt. Eba. The calculation results are very close to the case where the silent flight started one second earlier.

This difference in arrival time can be explained by the difference between dark and silent flights. The results suggest that after the SRC became optically transparent and entered dark flight, it remained acoustically opaque for

Downloaded from https://academic.oup.com/pasj/advance-article/doi/10.1093/pasj/psab126/6527740 by CNRS - ISTO user on 22 February 2022

about one second, travelling about 10 km before entering silent flight.

5 Conclusion

This study used data from 28 sensors installed at locations over which the Hayabusa2 SRC passed to investigate the infrasound generated by the SRC as it travelled at supersonic speed through the atmosphere. Based on an analysis of the arrival time of the observed infrasound, the trajectory of the SRC was calculated. The existence of silent flight was suggested for obtaining more accurate results. The azimuth of the trajectory of the SRC from the north is 41°.5 (counterclockwise) and the elevation angle was 5°.5. The capsule passed through the atmosphere and emitted a shock wave until it was about 39 km above the ground, at which point it began silent flight. The results suggest that the behavior of an object moving supersonically in the atmosphere can be determined from infrasound observations at multiple sites with a certain degree of accuracy. The calculated trajectory is consistent with JAXA's report and with optical observation and suggests that there is a sounding path (without light emission) of about 10 km for about one second before subsonic. Infrasound observations can be performed even in cloudy weather and daytime, and do not require any radio signals from the object. They are thus expected to play a role in the tracking of future atmospheric re-entry objects.

Acknowledgments

Although the Japanese infrasound team could not go to Australia because of COVID-19 restrictions, volunteers made the observation a success. We would like to thank Martin Cupák and the DFN team as well as Geoffrey Bonning, Andrew Cool, Karen Donaldson, Glyn Donaldson, Michael Roche, Terrence Wardle, and Yuta Hasumi for their support, without which this study would not have been finished. We are also indebted to JAXA's Hayabusa2 Project Team. The authors are grateful for the support from Woomera Test Range, in particular Guy Mold and Colin Telfer; and the Defence Science and Technology Group, in particular Kruger White and team.

Funding

This research was made possible largely through grants from The Murata Science Foundation (grant number M20AN115) and NEXCO Group Companies' Support Fund to Disaster Prevention Measures on Expressways. MYY would like to acknowledge their support from both fundings. The Desert Fireball Network team is funded by the Australian Research Council under grant DP200102073. EKS would like to acknowledge funding from the Institute of Geoscience Research and the Curtin Faculty of Science and Engineering.

Conflict of interest

The authors declare no conflict of interest.

References

Batubara, M., & Yamamoto, M.-Y. 2020, Remote Sensing, 12, 728
Ceplecha, Z., Borovička, J., Elford, W. G., ReVelle, D. O., Hawkes, R. L., Porubčan, V., & Šimek, M. 1998, Space Sci. Rev., 84, 327
Desai, P. N., Mitcheltree, R. A., & Cheatwood, F. M. 1999, in AAAF Int. Symp. on Atmospheric Reentry Vehicles and Systems, Paper No. 15.1 (Paris: Association Aéronautique et Astronautique de France)
Garcés, M. A., Hansen, R. A., & Lindquist, K. G. 1998, Geophys. J. Int., 135, 255
Hamama, I., & Yamamoto, M.-Y. 2021, Sensors, 21, 894
Ishihara, Y., Furumoto, M., Sakai, S., & Tsukada, S. 2004, Geophys. Res. Lett., 31
Ishihara, Y., Hiramatsu, Y., Yamamoto, M.-Y., Furumoto, M., & Fujita, K. 2012, Earth, Planets, Space, 64, 655
Ishihara, Y., Tsukada, S., Sakai, S., Hiramatsu, Y., & Furumoto, M. 2003, Earth, Planets, Space, 55, e9
Langston, C. A. 2004, J. Geophys. Res., 109, B12309
Lonzaga, J. B., Waxler, R. M., Assink, J. D., & Talmadge, C. L. 2015, Geophys. J. Int., 200, 1347
McCrosky, R. E., & Ceplecha, Z. 1970, Bull. Astron. Inst. Czech., 21, 271
Nagasawa, K. 1987, Bull. Earthq. Res. Inst. Univ. Tokyo, 62, 579
ReVelle, D., & Edwards, W. 2007, Meteorit. Planet. Sci., 42, 271
ReVelle, D., Edwards, W., & Sandoval, T. 2005, Meteorit. Planet. Sci., 40, 895
ReVelle, D. O. 1976, J. Geophys. Res., 81, 1217
Saito, H., Yamamoto, T., Nakajima, K., Kuramoto, K., & Yamamoto, M.-Y. 2021, J. Acoustical Soc. Am., 149, 591
Sansom, E., et al. 2022, PASJ, 74, 50
Tsuda, Y., Saiki, T., Terui, F., Nakazawa, S., Yoshikawa, M., & Ichiro Watanabe, S. 2020, Acta Astronaut., 171, 42
Tsuda, Y., Yoshikawa, M., Saiki, T., Nakazawa, S., & Watanabe, S. 2019, Acta Astronaut., 156, 387
Yamada, M., & Mori, J. 2012, Earth, Planets, Space, 64, 27
Yamamoto, M.-Y., Ishihara, Y., Hiramatsu, Y., Kitamura, K., Ueda, M., Shiba, Y., Furumoto, M., & Fujita, K. 2011, PASJ, 63, 971

Downloaded from https://academic.oup.com/pasj/advance-article/doi/10.1093/pasj/psab126/6527740 by CNRS - ISTO user on 22 February 2022